



CHALMERS
UNIVERSITY OF TECHNOLOGY

All-electrical creation and control of spin-galvanic signal in graphene and molybdenum ditelluride heterostructures at room temperature

Downloaded from: <https://research.chalmers.se>, 2021-08-31 12:22 UTC

Citation for the original published paper (version of record):

Hoque, A., Khokhriakov, D., Zollner, K. et al (2021)

All-electrical creation and control of spin-galvanic signal in graphene and molybdenum ditelluride heterostructures at room temperature

Communications Physics, 4(1)

<http://dx.doi.org/10.1038/s42005-021-00611-6>

N.B. When citing this work, cite the original published paper.

All-electrical creation and control of spin-galvanic signal in graphene and molybdenum ditelluride heterostructures at room temperature

Anamul Md. Hoque¹ , Dmitrii Khokhriakov¹ , Klaus Zollner², Bing Zhao¹, Bogdan Karpiak¹, Jaroslav Fabian²  & Saroj P. Dash^{1,3}  

The ability to engineer new states of matter and control their spintronic properties by electric fields is at the heart of future information technology. Here, we report a gate-tunable spin-galvanic effect in van der Waals heterostructures of graphene with a semimetal of molybdenum ditelluride at room temperature due to an efficient spin-charge conversion process. Measurements in different device geometries with control over the spin orientations exhibit spin-switch and Hanle spin precession behavior, confirming the spin origin of the signal. The control experiments with the pristine graphene channels do not show any such signals. We explain the experimental spin-galvanic signals by theoretical calculations considering the spin-orbit induced spin-splitting in the bands of the graphene in the heterostructure. The calculations also reveal an unusual spin texture in graphene heterostructure with an anisotropic out-of-plane and in-plane spin polarization. These findings open opportunities to utilize graphene-based heterostructures for gate-controlled spintronic devices.

¹Department of Microtechnology and Nanoscience, Chalmers University of Technology, Göteborg, Sweden. ²Institute for Theoretical Physics, University of Regensburg, Regensburg, Germany. ³Graphene center, Chalmers University of Technology, Göteborg, Sweden. ✉email: saroj.dash@chalmers.se

The spin-orbit interaction (SOI) is the fundamental physical phenomenon and pivotal for state-of-the-art spintronics and quantum technologies^{1–4}. Specifically, the SOI is the origin of fascinating effects like current-induced transverse spin polarization in non-magnetic materials, known as spin Hall effect (SHE) in bulk, Rashba-Edelstein effect (REE) at the heterostructure interfaces, and spin-momentum locking (SML) in topological materials⁵. Recent experiments utilizing the charge-to-spin conversion (CSC) and its inverse effects have been performed on metallic multilayers⁶, semiconductors², oxide heterostructures^{7,8}, two-dimensional (2D) materials^{9,10}, van der Waals (vdW) heterostructures with graphene (Gr)^{11–17}, and the topological insulators^{18,19}. Such SOI-induced charge-spin conversion features are promising for all-electrical spin-orbit torque-based technology^{1–4}.

Recently discovered topological Weyl semimetals (WSMs) were predicted to provide a much larger CSC efficiency, giant REE²⁰ and SHE²¹, due to their non-trivial band structure in both bulk and surface states. The type-II WSMs, such as tungsten ditelluride (WTe₂) and molybdenum ditelluride (MoTe₂) possess strong SOI and band structure with a large Berry curvature and spin-polarized bulk and surface states up to room temperature^{22,23}. Furthermore, the CSC in WSMs is of great interest in its own^{9,15,24–28}, but their true potential lies in forming vdW heterostructures with graphene. It has been predicted that the addition of a graphene layer on topological materials can even enhance the REE by orders of magnitude^{29–32}, which can be due to different proximity-induced interactions in the heterostructures, such as Kane-Mele SOI, spin-valley coupling, and Bychkov-Rashba interaction^{30,33}. Recently, charge-spin conversion effects are also reported in Gr-TMD heterostructure^{34,35} and also in low-symmetry semimetal WTe₂^{15,26}, with both conventional and unconventional nature. Moreover, an interesting energy-dependent spin texture and giant CSC efficiency are also expected to be present in semimetal-graphene heterostructures. The much-needed experimental proof of such gate tunable charge-spin conversion effect in graphene-semimetal vdW heterostructure would considerably boost the chance of its utilization in emerging spintronic technologies.

Here, we report the creation of proximity-induced spin-galvanic effect (SGE) in vdW heterostructures of semimetal MoTe₂ and graphene. This article demonstrates a proximity-driven SOI mechanism, the Rashba-Edelstein effect (REE), in the vdW heterostructure-based spintronic device to achieve spin-to-charge conversion (SCC) with high efficiency. The magnitude and the sign of the spin-galvanic signal can be controlled by applying gate voltage near the charge neutrality point, which is understood based on our density functional theory (DFT) calculations showing SOI-induced spin-split electronic band structure of the graphene in the heterostructure. We also performed measurements in geometries where the injector ferromagnet is placed perpendicularly to the Gr-MoTe₂ heterostructures, showing the REE-induced spin-switch and Hanle spin precession signals. These results highlight the unique possibility of achieving efficient gate tunability of the SGE in vdW heterostructure.

Results

We have chosen semimetal MoTe₂ as the high SOI material, which has gained growing interest regarding its topological properties in the T_d phase. The MoTe₂ is verified as the first type-II WSM, where tilted Weyl cones exist in pairs as the contact point between electron and hole pockets, which are connected by a spin-polarized Fermi arc surface states^{23,36,37}. Our basic measurements of temperature dependence (Supplementary Fig. S1) together with the Raman spectrum (Supplementary Fig. S2) of MoTe₂ show the metallic 1 T'

phase of the material at room temperature³⁸. Because of the ability to create designer heterostructure of various layered materials^{39,40}, we prepare the heterostructure of multilayer MoTe₂ of thickness 43 nm (Supplementary Fig. S3) and monolayer chemical vapor deposited (CVD) graphene^{41,42} by dry transfer method inside a glovebox.

The hybrid spintronic devices were nanofabricated in Hall-bar-shaped geometry with multiple contacts to detect the SGE. Measurements were performed in various device geometries such as magnetization rotation, spin switch, and Hanle spin precession methods. First, we present results from magnetization rotation experiments in a device where the ferromagnetic contact is placed parallel to the graphene-MoTe₂ heterostructures, as shown in the schematics and the device picture (Fig. 1a and b). The device consists of Hall-bar shaped Gr-MoTe₂ heterostructure region for spin-to-charge conversion, graphene channel for spin transport, Co/TiO₂ ferromagnetic contacts (FM) on graphene for spin injection (contact 1 in Fig. 1b), and Ti/Au contacts (contact 3 & 4 in Fig. 1b) on graphene for detection of the voltage signal and also as reference electrodes (contact 2 in Fig. 1b), and Si/SiO₂ substrate acts as a global back gate. To be noted, the contacts (3 & 4) are made explicitly on graphene to detect the proximity-induced effects. This is in contrast to the devices used in Zhao, B. et al.^{12,15,26}, where the contacts are made on WTe₂ flake to measure spin Hall effects (SHE) in WTe₂, and no proximity effect could be detected. The contact resistances of FMs on graphene are about 5–8 kΩ and the channel mobility of Gr-MoTe₂ heterostructure is estimated to be about 2200 cm²V⁻¹s⁻¹ at room temperature.

The basic spin transport measurements were carried out at room temperature using FM injector and detector tunnel contacts in the pristine graphene ($L_{\text{ch}} = 5.7 \mu\text{m}$) and Gr-MoTe₂ heterostructure regions ($L_{\text{ch}} = 6.7 \mu\text{m}$), as depicted in Supplementary Fig. S4. The spin transport in pristine graphene shows 200 mΩ of spin-valve signal and corresponding Hanle measurements provide an estimated spin lifetime of ~ 185 ps; on the other hand, no spin transport signal could be observed through the Gr-MoTe₂ heterostructure region. This disappearance of the spin signal across the heterostructure can be either due to spin absorption by MoTe₂ or the creation of a strong SOI and band structure hybridization in the Gr-MoTe₂ heterostructure. Although the spin absorption effect by MoTe₂ cannot be ruled out, the measured gate tunable spin galvanic signal presented below does not indicate the contribution of charge-spin conversion from only MoTe₂, but to be originating from the proximitized graphene. As predicted for graphene-transition metal dichalcogenides (TMD) heterostructure³³, graphene in proximity to MoTe₂ can also acquire strong SOI and a spin texture with a Rashba spin-split in conduction and valence bands with the same spin chirality (Fig. 1c), which can be probed by tuning the Fermi level (E_f) using a gate voltage.

Proximity-induced spin-galvanic effect. The charge-spin conversion due to the proximity-induced SOI in Gr-MoTe₂ heterostructure can be measured by employing a direct REE or its inverse phenomenon (IREE) based methods⁵. The charge current-induced REE can be detected by a FM contact due to charge-to-spin conversion. In contrast, for the IREE measurements, a spin current is injected from a FM into a heterostructure region and, consequently, a voltage signal is measured due to a spin-to-charge conversion. Figure 1a shows the schematics of the NL measurement geometry used for the detection of SGE in the IREE measurement geometry. In this hybrid spintronic device, the spin current is injected from a FM contact into the graphene channel and diffused into the Gr-MoTe₂ heterostructure, and

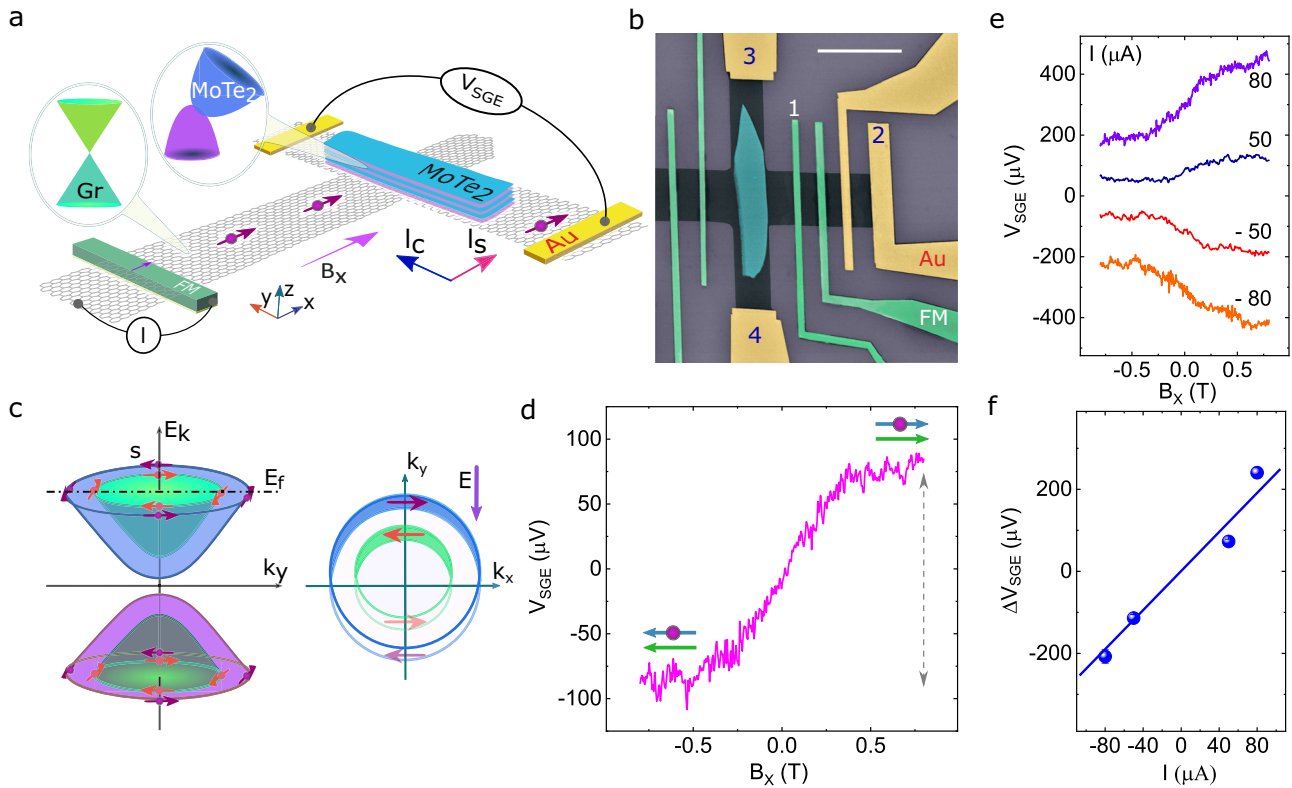


Fig. 1 Proximity-induced spin-galvanic effect in graphene-MoTe₂ van der Waals heterostructure at room temperature. **a, b** The spintronic device schematics with the measurement scheme and colored scanning electron microscope (SEM) image consisting of graphene (gray)/MoTe₂ (blue) heterostructure on Si/SiO₂ substrate, ferromagnetic (FM) and non-magnetic (Ti/Au) contacts on graphene. The scale bar in the SEM image is 6 μm. **c** A schematic band diagram of modified graphene in a heterostructure with MoTe₂, showing Rashba spin-split conduction and valence bands in accordance with the energy in momentum space (E_k), where Fermi energy (E_f) is in the conduction band. Application of an electric field with such spin texture is expected to create a spin accumulation due to the Rashba-Edelstein effect (REE), and inversely, a spin accumulation can be converted to a charge voltage via inverse Rashba-Edelstein effect (IREE). **d** Measured spin-galvanic effect as a non-local voltage (V_{SGE}) signal due to IREE by injecting a spin current (I_s) from a FM into the graphene-MoTe₂ heterostructure region. A change in V_{SGE} is measured by sweeping a magnetic field along the x-axis (B_x) with an application of $I = 80 \mu\text{A}$, the gate voltage $V_g = -10\text{V}$ in Dev 1 at room temperature. The green and blue arrows denote the FM magnetization and direction of the diffused spin into the graphene-MoTe₂ heterostructure, respectively. **e, f** Measured bias dependence of V_{SGE} signal and its magnitude ΔV_{SGE} as a function of bias current in Dev 1. A linear background is subtracted from the data and shifted in the y-axis for clarity. The line is the linear fit to the data in **f**. The error bars are calculated from the noise level of the manifested signals and not clearly visible because error bars are smaller than the data points.

finally detected as a voltage signal (V_{SGE}) across the Hall-bar structure with non-magnetic Ti/Au contacts on graphene. Due to the IREE in the Gr-MoTe₂ heterostructure region with a possibility of spin-split bands (Fig. 1c), the diffused spin-polarized carriers create a non-equilibrium spin density across the heterostructure with a net momentum along the $\pm y$ -axis depending on the spin direction ($\pm s$). This is detected as a voltage signal, V_{SGE} ($I_c \propto z \times n_s$ (I_s); here, I_c , z and n_s are the induced charge current, out-of-plane direction non-equilibrium spin density accumulated via spin current I_s , respectively). The direction of the injected spin (in $\pm x$ -direction) and hence the V_{SGE} is controlled by sweeping a magnetic field in the x-direction ($\pm B_x$), which induces spin precession together with rotation and saturates the magnetization of the injector FM (Fig. 1d). The spin precession due to the applied x-field ($\pm B_x$) will be in the y - z plane, and the projection of spin polarization along the x -axis will be the same during the spin precession. Nevertheless, the accumulated non-equilibrium spin density (n_s) depends on the spin direction towards the x -axis ($\pm x$) in our measurement system of IREE. Due to the unchanged spin projection along the x -axis during the spin precession, together with changing magnetization of the injector FM contact, the resulting IREE signal increases with B_x until the saturation of FM magnetization (0.4 T) without any contribution of spin precession. Accordingly, the measured V_{SGE} increases in the low field

range and saturates at magnetic fields above $B \approx \pm 0.4\text{ T}$ (see Supplementary Fig. S5, where a x-Hall measurement shows the saturation field of the FM contact). A giant spin-galvanic signal has been obtained at room temperature with an amplitude up to $\Delta R_{SGE} = \Delta V_{SGE}/I \sim 4.96 \Omega$ (with $I = -80 \mu\text{A}$ at $V_g = 40\text{ V}$) and lower bound of the efficiency (α_{RE}) of IREE is estimated to be 7.6% by using the Eq. (1)^{17,34}.

$$\alpha_{RE} = \frac{\Delta R_{SGE}}{2\rho_G} \frac{w_{MoTe_2}}{P \lambda_G \left(e^{-\frac{L}{\lambda_G}} - e^{-\frac{L+w_{MoTe_2}}{\lambda_G}} \right)} \quad (1)$$

Here, ΔR_{SGE} , P , w_{MoTe_2} (2.3 μm), λ_G (2.65 μm), ρ_G (1.6 kΩ), and L (3.37 μm) are the signal amplitude, the spin polarization of Co/TiO₂ contact (considering 10%, see Supplementary Fig. S6), the width of the MoTe₂ flake, spin diffusion length, channel resistivity, and channel length, respectively. Here, we consider the spin diffusion length of the pristine graphene region since no spin precession signal is observed in the Gr-MoTe₂ heterostructure region. However, we would like to mention that the estimated α_{RE} is the lower limit as the spin diffusion length in Gr-MoTe₂ heterostructure is smaller due to the enhanced SOI. This magnitude of the observed R_{SGE} and α_{RE} is found to be larger than the previous results on 2D materials heterostructures^{16,17}.

We can also electrically tune the magnitude and sign of the SGE signal with the spin injection bias current I . In our measurement configuration, changing the bias current on the FM spin injector contact changes the direction of accumulated spin polarization in the graphene channel. Hence, with a change in the non-equilibrium spin density, the direction of the measured V_{SGE} that is induced by IREE also changes (Fig. 1e). To be noted, the bias current $+I$ corresponds to spin injection from the FM into the graphene channel, and $-I$ correspond to the spin extraction condition. The bias dependence of measured V_{SGE} signal amplitude in the range of $I = -80 \mu\text{A}$ to $80 \mu\text{A}$ has been depicted in Fig. 1f, along with a linear fit to the data points. We also observed inverse SGE (ISGE), following the reciprocity relation, where charge current is applied with Ti/Au contacts across Gr-MoTe₂ heterostructure Hall-cross and non-local voltage (V_{nl}) is measured in graphene channel with FM detector contact (Supplementary Fig. S7).

Angle dependence of the spin-galvanic signal. Next, the angular dependence of the measured NL voltage signal was performed at room temperature. The measurements were manifested by varying the angle (θ) of the applied in-plane (x - y plane) magnetic field (B) direction with respect to the x -axis, illustrated by the schematics and measurement geometry in Fig. 2a. The measured V_{SGE} changes with the effective component of B in the x -direction as depicted in Fig. 2b in Dev 2 ($L_{ch} = 5 \mu\text{m}$) with an injection bias current of $I = 60 \mu\text{A}$. No spin-galvanic signal is detected when the

B is aligned with the y -axis ($\theta = 90^\circ$) because at this stage, the injected spins remain parallel to the B field and no spin precession is taking place in the measurement geometry. The sign of the V_{SGE} reverses gradually in between $\theta = 0^\circ$ to 180° (π) due to changing the FM magnetization direction along ($\pm x$ -axis) and associated reversal of the injected spin orientation.

In contrast to the Gr-MoTe₂ heterostructure, no such features have been observed in control samples of only graphene Hall-cross, with measurement geometry shown in the inset of Fig. 2c. Figure 2c shows the null non-local signal (V_{nl}) measured in pristine graphene Hall-cross at room temperature with $I=100 \mu\text{A}$, $V_g = -50 \text{V}$ for different measurement angles. The magnitude of the measured SGE signals (ΔV_{SGE}) in the Gr-MoTe₂ heterostructure and non-local signal in the only graphene (ΔV_{nl}) as a function of the measurement angle θ are shown in Fig. 2d, following the expected behavior, where the induced voltage V_{SGE} ($I_c \propto z \times n_s (I_s)^{15,43}$). The angle dependence data of the ΔV_{SGE} is found to follow the $\cos(\theta)$ function, which establishes the relation between the direction of the injected spin-current and the induced SGE in the Gr-MoTe₂ heterostructure. On the other hand, the ΔV_{nl} in only graphene Hall-cross renders the null signal with the applied magnetic field direction, which rules out the effect of the stray field from the FM electrodes to be the origin of the manifested SGE signal in the Gr-MoTe₂ heterostructure.

Gate-controlled switching of spin-galvanic signal. In order to demonstrate the electric field-controlled switching of the SGE, we

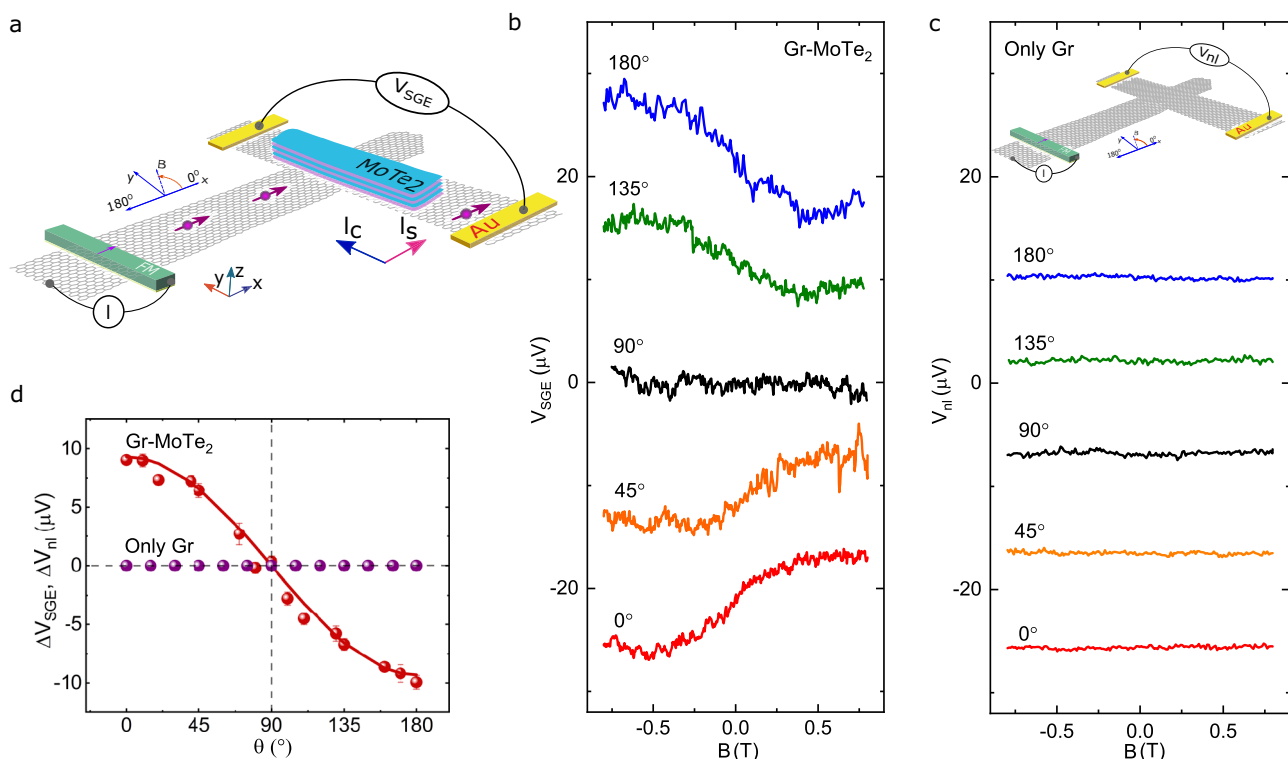


Fig. 2 Angle dependence of spin-galvanic signal in the graphene-MoTe₂ heterostructure. **a** A schematic illustration of the spin-galvanic signal measurement geometry with directions of an applied magnetic field (B), the injector ferromagnet magnetization (M), the spin current (I_s), and external magnetic field angle (θ) in x - y plane. **b** The manifested spin-galvanic signal (V_{SGE}) as a function of the magnetic field (B) sweep for various measurement angle (θ) orientations in the x - y plane, with an application of $I = 60 \mu\text{A}$ in Dev 2 at room temperature. A linear background is subtracted from the data and shifted in the y -axis for clarity (see Supplementary Fig. S8). **c** As a control experiment, the non-local signal as a function of magnetic field sweep (B) for various in-plane (x - y plane) measurement angle (θ) orientations in only graphene Hall cross at room temperature with $I=100 \mu\text{A}$ and $V_g = -50 \text{V}$ along with the measurement geometry in the inset. The signals are shifted in the y -axis for clarity. **d** The magnitude of spin-galvanic signals (ΔV_{SGE}) in graphene-MoTe₂ heterostructure and non-local signal (V_{nl}) in the only graphene as a function of the applied magnetic field angle (θ). The solid line is the $\cos(\theta)$ function. The error bars are calculated from the noise level of the manifested signals and not clearly visible because error bars are smaller than the data points.

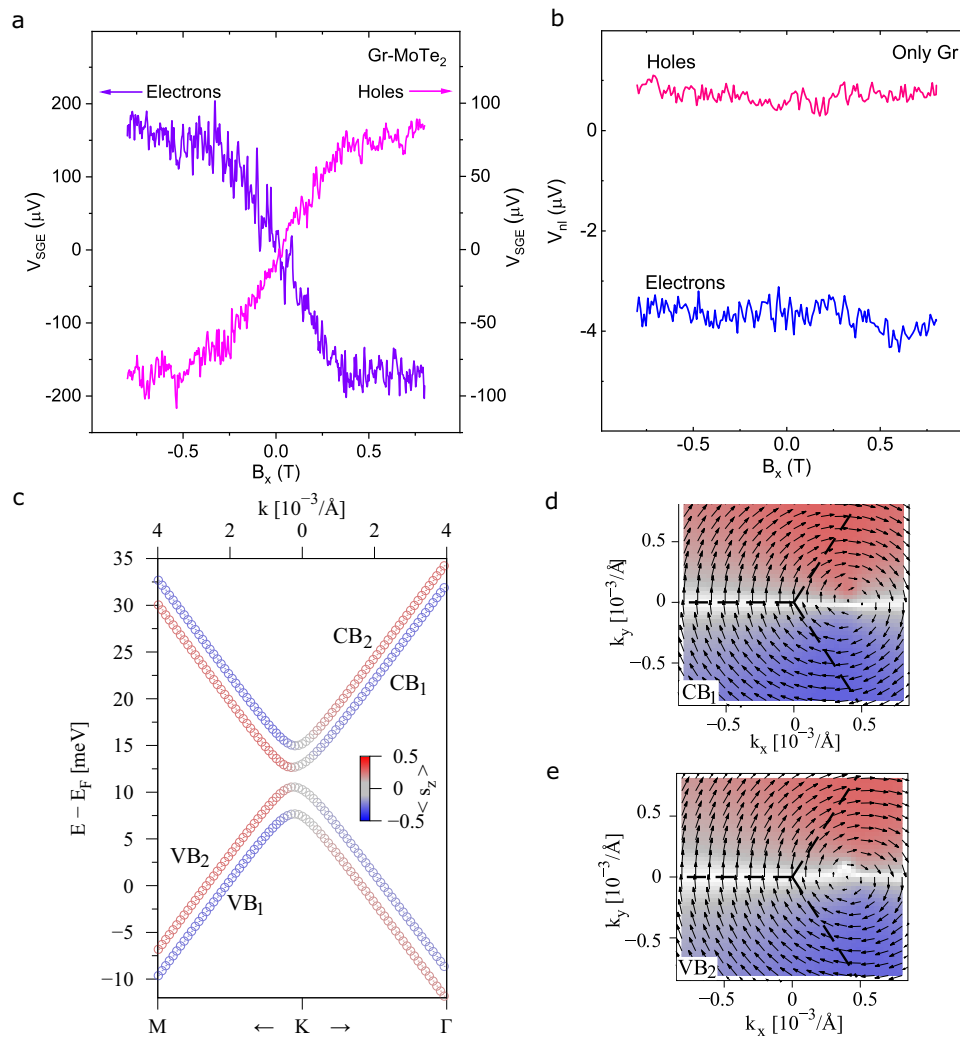


Fig. 3 Gate-controlled switching of spin-galvanic signal in graphene-MoTe₂ heterostructure at room temperature. **a** Measured spin-galvanic signal (V_{SGE}) by sweeping a magnetic field along the x -axis (B_x) at room temperature in graphene-MoTe₂ heterostructure (Dev 1) with $I = 80 \mu\text{A}$ and applied gate voltages of $V_g = 20 \text{ V}$ and -10 V to position the Fermi level (E_F) in the electron and hole doping regimes, respectively. A linear background is subtracted from the data (see Supplementary Fig. S9). **b** Measured non-local signals (V_{nl}) in pristine graphene Hall cross by sweeping a magnetic field in the x -direction (B_x) for electron- and hole-doped regions with $I = 100 \mu\text{A}$, $V_g = 70 \text{ V}$ and -50 V , respectively. **c** The low energy band structure of graphene in proximity to MoTe₂ from density functional theory calculations. The color is the expected value of the spins polarized along with the z -direction (s_z). **d, e** Density functional theory calculations for similar clockwise spin texture in the outermost conduction (e_1^{CB}) and valence band (e_2^{VB}) in graphene-MoTe₂ heterostructure.

measured SGE for the electron (n) and hole (p) doped regimes of the Gr-MoTe₂ heterostructure. The applied gate voltage modulates the Fermi level (E_F) position in the Gr-MoTe₂ hybrid bands for probing the spin-split REE-induced non-equilibrium spin accumulation (n_s) with different charge carrier types. Figure 3a shows the opposite signs of V_{SGE} signals for two different doping regimes, electrons (violet) at $V_g = 20 \text{ V}$ and holes (magenta) at $V_g = -10 \text{ V}$ at room temperature. Control experiments with gate dependence of standard Hanle spin precession signals (Supplementary Fig. S6) confirm that the sign change in SGE is not due to a change in the sign of spin polarization of the injector FM contacts. The proximity-induced REE effect in graphene is predicted to be dependent on the conduction charge carrier type, i.e., electrons and holes, since spin polarity in Rashba contour remains unchanged in valence and conduction bands, unlike the spin-momentum locking in topological insulators^{33,44}. The observed IREE produces a charge current ($I_c \propto z \times n_s$) perpendicular to the injected spin densities (n_s), which changes its

direction because of a unidirectional accumulation of electron and holes ($-q$ for electrons and $+q$ for holes) in the heterostructure with specific spin orientations. So, it can be concluded that the measured SGE signal and the sign change of the V_{SGE} is inherently due to induced IREE in Gr-MoTe₂ heterostructure. Similar gate-dependent sign change behavior of SGE is also observed in Dev 2 (see Supplementary Fig. S10). To compare the induced SGE in Gr-MoTe₂ with pristine graphene, NL signals (V_{nl}) are measured for electron- and hole-doped regions, depicted in Fig. 3b, with $I = 100 \mu\text{A}$ at $V_g = 70 \text{ V}$ and -50 V , respectively. The resultant signals can be considered as null noise-signals because of the absence of REE in pristine graphene.

To understand our experimental findings of SGE, we have performed a DFT calculation of the electronic band structure of Gr-MoTe₂ heterostructure to identify the Rashba spin texture and to verify the enhanced SOI strength in the heterostructure (Supplementary Note 1 for details)^{45,46}. A side and top view of the geometry used for band structure calculations are shown in

Supplementary Fig. S13. The low energy band structure of the graphene and 1 T'-MoTe₂ heterostructure is presented in Fig. 3c and we found four states ($\epsilon_{1/2}^{VB/CB}$) of Rashba spin-splitting with SOI strength of around 2.5 meV (see Supplementary Fig. S15). We also noticed that the bands display a clear signature of Rashba SOI, as the spin in the outermost conduction (ϵ_1^{CB}) and valence band (ϵ_2^{VB}) is aligned clockwise (Fig. 3d, e), while the corresponding spin-orbit split partner bands (for example, ϵ_1^{CB} and ϵ_2^{CB}) show a counter-clockwise sense of spin-alignment (Supplementary Fig. S16). The calculations have also revealed an unusual proximity-induced spin texture in graphene: the out-of-plane spin polarization is highly anisotropic around K, and the in-plane spin polarization (Rashba) vortex is shifted from K'. Such a spin texture in the graphene valence and conduction band in the heterostructure can explain our measured SGE signal, where the sign of the SGE signal is efficiently controlled by the application of a gate voltage.

Interestingly, the gate electric field is changing simultaneously the spin properties (SOI and Rashba effect) and carrier concentration and type in the Gr-MoTe₂ heterostructure. To estimate the overall effect of SOI, we have theoretically calculated the splitting of low energy band due to SOI (ΔE_{so}) in Gr-MoTe₂ heterostructure at various electric fields (see Supplementary Fig. S18 in the Supplementary Note 2 for details). We found that the splitting of the low energy bands in the Gr-MoTe₂ interface and the doping can be tuned by the electric field. Theoretically, we found that for the negative field (-2 V/nm), where graphene is electron-doped, the splitting (i.e., Rashba SOI) is larger than for the positive field (2 V/nm), where graphene is hole-doped. Our measurements also show that the signal amplitude (ΔV_{SGE}) is higher for electrons compared to holes, which is in agreement with the theoretical analysis. However, experimentally we only applied about ± 0.50 V/nm and a very negligible modulation of Rashba SOI is expected within this applied electric field range. In addition to a small change of Rashba SOI with the electric field, the gate voltage also changes the Fermi level in Gr-MoTe₂ heterostructure significantly (hence, the charge of carrier type), which gives rise to the sign change of the SGE signal.

Systematic gate dependence of V_{SGE} is measured at different gate voltages (V_g) in the range from -40 to +40 V for two different spin injection bias currents $I = \pm 80 \mu\text{A}$ at room temperature (Fig. 4a). It can be observed that the SGE signal changes sign with gate voltage and spin injection bias currents. To correlate the sign change behavior of the SGE signal with the carrier type of the Gr-MoTe₂ heterostructure, the gate dependence of graphene channel resistance (R_{Gr}) is plotted together with ΔV_{SGE} and ΔR_{SGE} . To be noted, the R_{Gr} is measured for the channel length of 6.7 μm (Fig. 4b inset), which includes part of the graphene region that is not contributing to the SGE signal. Therefore, the charge neutrality point (CNP) for the only Gr-MoTe₂ heterostructure region can be between 10–20 V. Interestingly, the gate dependence of SGE signal ΔV_{SGE} and ΔR_{SGE} change sign around the charge neutrality point, which is between 10–20 V. Opposite signs of the SGE signals are consistently observed for carriers in the electron- and hole-doped regimes of the heterostructure, i.e. for the conduction and valence bands of the hybrid structure. The signal amplitudes ΔV_{SGE} , ΔR_{SGE} , and corresponding α_{RE} (Supplementary Fig. S11) are also found to be asymmetric, higher for an electron-doped regime compared to the hole-doped regime. Such behavior can be due to the different doping regimes and spin-charge conversion efficiency.

Spin-galvanic signal detection via spin switch and spin precession. To substantiate the proximity-induced SGE in Gr-MoTe₂ heterostructure via spin-switch and Hanle spin precession

measurements¹¹, a different device is fabricated (Supplementary Fig. S12a) where an injector FM is placed perpendicular (x -axis) to the heterostructure. At first, the spin transport properties in graphene across the Gr-MoTe₂ heterostructure have been verified. Figure 5a depicts the schematic of the device and measurement geometry to measure the non-local spin signal with a FM detector in graphene across the Gr-MoTe₂ heterostructure. The non-local spin valve (V_{nl}) in graphene is depicted in Fig. 5b with $I = -300 \mu\text{A}$ at $V_g = -50\text{V}$, where the magnetic field is applied along the easy axis of the injector's magnetization (x -axis). The Hanle spin precession signal in graphene is presented in Fig. 5c with $I = -50 \mu\text{A}$ at $V_g = -50\text{V}$. The characteristic switching in spin-valve and antisymmetric Hanle are due to the perpendicular magnetization of the injector (x -axis) and detector (y -axis) FM contacts. Next, the non-local SGE signal in the Gr-MoTe₂ has been investigated. Figure 5d shows the schematic of the device and measurement geometry to measure non-local SGE signal (V_{SGE}) with Ti/Au contacts along the Hall-cross of Gr-MoTe₂ heterostructure. In this measurement geometry, it is expected that applying a changing magnetic field along the easy axis (x -axis) of the FM injector should have manifested a spin switch signal across the Hall-cross due to proximity-induced SGE. The SGE signal with varying in-plane magnetic field (B_x) at room temperature is presented in Fig. 5e with $I = -100 \mu\text{A}$ at $V_g = -50\text{V}$. As the graphene channel was highly doped in this device, a complete gate-dependent measurement could not be performed, as the signal became noisy at positive gate voltages. The full bias dependence of SGE signals is presented in Supplementary Fig. S12. As a confirmation of the spin-related origin of the observed SGE, Hanle spin precession with out-of-plane field B_z is measured and shown in Fig. 5f along with fitting for $I = -100 \mu\text{A}$ at $V_g = -50\text{V}$. The spin lifetime and spin diffusion length in Gr-MoTe₂ heterostructure are extracted to be around $\tau_s = 20\text{ps} \pm 1\text{ps}$ and $\lambda_s = 155\text{nm} \pm 5\text{nm}$.

Discussion

The observed SGE in Gr-MoTe₂ heterostructure can have interesting microscopic origins. Although topologically non-trivial Weyl states in MoTe₂ are found to exist at low temperature²⁷, the trivial spin-polarized surface and bulk states are also shown to exist in these materials even at room temperature²³. Additionally, the existence of polar instability near the surface is also observed even when the MoTe₂ bulk is in a centrosymmetric phase^{23,36}. Therefore, the surface states of MoTe₂ can have a strong influence on the band hybridization and proximity-induced spin-charge conversion properties of Gr-MoTe₂ heterostructure. Additionally, our calculations show the presence of a very strong SOI with band splitting of a few meV in graphene in proximity with MoTe₂, similar to the predictions on graphene-semiconducting TMD heterostructure^{30,47}. Interestingly, the induced Rashba spin-split bands in graphene should have opposite spin polarization with a helical spin texture due to the lack of inversion symmetry at the interface, which is protected by time-reversal symmetry^{4,33}. Moreover, this proximity-induced band splitting in graphene is predicted to emanate along the energy axis with an in-plane spin polarization, which is the cardinal aspect for a novel spin-to-charge conversion effects⁴⁷. The in-plane spin accumulation in our measured Gr-MoTe₂ heterostructures renders this SGE signal to be due to proximity-induced IREE in graphene. It can be affirmed that the polarization of the accumulated spins is in-plane; otherwise, a signal would have been observed when the applied magnetic field direction is aligned with the y -axis ($\theta = 90^\circ$) in our angle dependence measurements^{16,17}.

In our measurements, we do not observe the contribution of SHE and REE from only MoTe₂ to the manifested gate-tunable

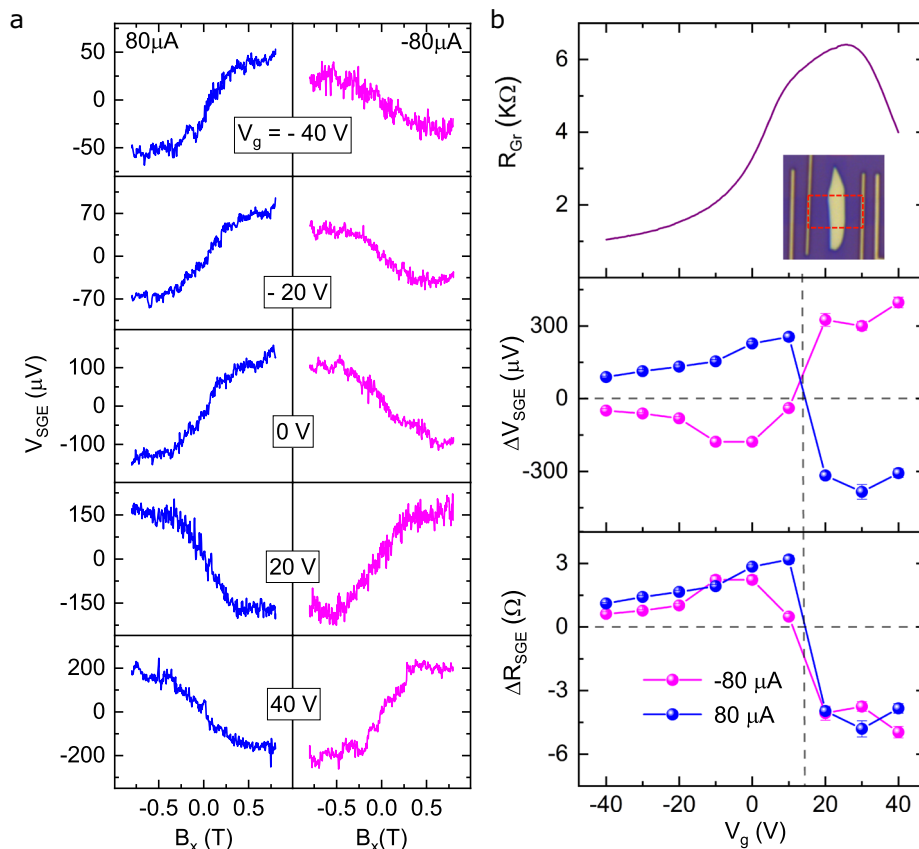


Fig. 4 Gate dependence of spin-galvanic signal in graphene-MoTe₂ heterostructure at room temperature. **a** Evolution of measured spin-galvanic signal (V_{SGE}) by sweeping magnetic field along the x -axis (B_x) at different gate voltages in the range of +40 to -40 V, with $I = \pm 80 \mu\text{A}$ in Dev 1 at room temperature. The sign of the spin-galvanic signal changes with gate voltage V_g and spin injection bias current I . **b** Gate dependence of graphene channel resistance (R_{Gr}) and spin-galvanic signals (ΔV_{SGE} and $\Delta R_{SGE} = \Delta V_{SGE}/I$) at $I = \pm 80 \mu\text{A}$ at room temperature. The sign change of the spin-galvanic signal is observed close to the charge neutrality point of graphene and the signals are of opposite sign for n and p -type regimes of the graphene-MoTe₂ heterostructure. The error bars are calculated from the noise level of the manifested signals and not clearly visible because error bars are smaller than the data points.

SGE signals, as the charge carriers in metallic MoTe₂ are not tunable by a gate voltage. We can also rule out proximity-induced SHE in graphene in a heterostructure with MoTe₂ since that would have polarized the spins in the z -direction, which would have resulted in a spin precession Hanle peaks near $B = 0$ T field, which are not observed¹⁶. We can exclude the thermal-related spin effects as the origin of the observed SGE signal for the reason that the sign of the SGE signal changes with the DC bias current direction, as depicted in Fig. 1e, as the temperature gradient in the heterostructure should not change with the bias direction. Moreover, we manifested the linear bias dependence of the SGE signal (Fig. 1f), while the thermal-related effect should be proportional to I^2 . In addition, we observe a gate dependence tuning of the SGE signal magnitude with a sign change for the electron- and hole-doped regimes of the Gr-MoTe₂ heterostructure. The effect of stray Hall effect in our SGE signal can be disregarded because of the larger channel length between the injector and detector, and higher magnitude of the obtained SGE signal, which is in the range of few Ohms where the magnitude of the stray Hall effect is estimated to be in the range of few milli-Ohms in a similar kind of device structure^{16,48}. The controlled experiments with only graphene channels show a null signal, further supporting the measurements. Moreover, spin-switch and Hanle spin precession measurements have been observed while injecting spin current by a FM injector perpendicular (x -axis) to the Gr-MoTe₂

heterostructure. So, the observed SGE is inevitably due to IREE in proximitized graphene because of proximity-induced SOI from MoTe₂.

In conclusion, we demonstrated the electrical detection and control of proximity-induced Rashba spin-orbit interaction in vdW heterostructures at room temperature. The observed SGE in the heterostructure of semi-metallic MoTe₂ and large-area CVD graphene can offer unique advantages for faster and low-power spin-charge conversion-based spintronic devices. Specifically, vdW heterostructure provides entirely new mechanisms for tuning emergent spin functionalities by an electric field, resulting from interfacial proximity interactions between the stacked layered materials. Due to the proximity effect, graphene acquires strong SOI and a spin texture with spin-split conduction and valence bands, which is ideal for tuning by a gate voltage. Controlling the magnitude and sign of the spin voltage by an external electric field at room temperature can be efficiently used for gate tunable spin-orbit torque (SOT) based magnetic random-access memory (MRAM)³ and logic technologies². The strong Rashba SOI in vdW heterostructures can further enable new energy-dependent spin textures by tuning their proximity-induced interactions and expected to provide a new playground for the creation of unique topological states of matter, for example, in heterostructures with layered ferromagnetic⁴⁹ and superconducting materials^{1,4}.

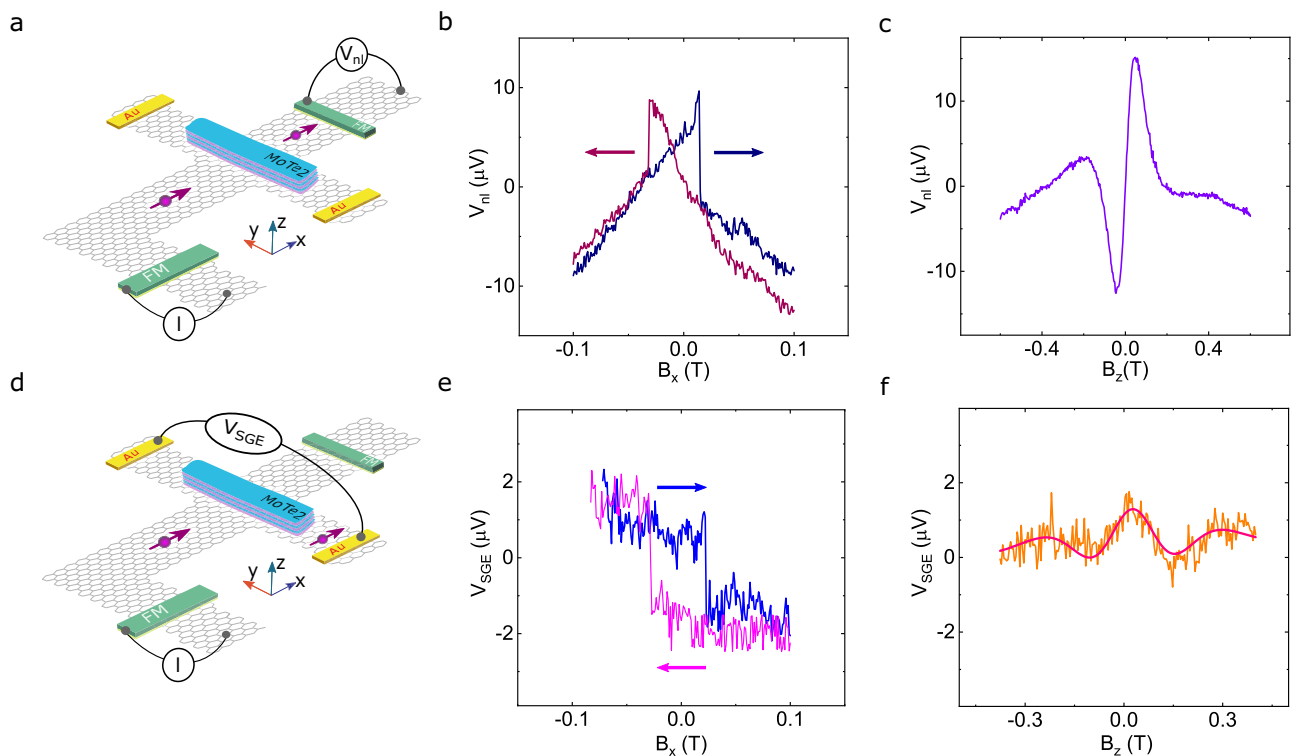


Fig. 5 Spin-galvanic signal with an injector ferromagnet (FM) perpendicular to the graphene-MoTe₂ heterostructure. **a** A schematic of the device and measurement geometry to measure the non-local spin signal with a ferromagnetic detector in graphene across the graphene-MoTe₂ heterostructure. **b, c** Spin valve and Hanle spin precession measurements, respectively. **d** A schematic of the device and measurement geometry to measure the non-local spin-galvanic signal (V_{SGE}) with non-ferromagnetic detectors (Ti/Au) along the Hall-cross of graphene-MoTe₂ heterostructure. **e** The spin-galvanic signal, V_{SGE} , is measured with varying in-plane magnetic field (B_x) at room temperature. **f** The spin-galvanic signal was detected via Hanle spin precession with varying out-of-plane magnetic field (B_z) along with Hanle fitting.

Methods

Device fabrication and measurements. The vdW heterostructures of Gr-MoTe₂ were fabricated by dry transfer of 1 T' MoTe₂ (from HQ Graphene) flakes on CVD graphene (from Groltux), onto SiO₂ (285 nm)/n-doped Si substrate using scotch tape method inside a glovebox in an inert atmosphere. The graphene and the Gr-MoTe₂ channels were patterned into Hall-bar-shaped structures by electron beam lithography and oxygen plasma etching. Both non-magnetic and ferromagnetic contacts to graphene were defined by two-step electron beam lithography and lift-off process. The non-magnetic contacts were prepared by deposition of 10 nm Ti and 60 nm Au by electron beam evaporation and lift-off process. For the preparation of ferromagnetic contacts to graphene, we used a two-step electron beam evaporation of 0.6 nm of Ti and in-situ oxidation, followed by a 90 nm of Cobalt (Co) deposition. The lift-off was performed in warm acetone and IPA. The spin-galvanic measurements were performed in a vacuum system with a magnetic field up to 0.8 Tesla and a sample rotation stage. All the electrical measurements were performed at room temperature using a current source Keithley 6221, a nano voltmeter Keithley 2182 A and Keithley 2612B source meter for application of gate voltages.

Density functional theory calculations. The electronic structure calculations and structural relaxation of our heterostructures are performed by means of density functional theory⁴⁶ within Quantum ESPRESSO⁴⁵. Self-consistent calculations are performed with the k -point sampling of $18 \times 18 \times 1$. We use an energy cutoff for charge density of $550 R_p$, and the kinetic energy cutoff for wavefunctions is $65 R_p$ for the fully relativistic pseudopotential with the projector augmented wave method⁵⁰ with the Perdew-Burke-Ernzerhof exchange-correlation functional⁵¹. For the relaxation of the heterostructures, we add van der Waals corrections^{52,53} and use a quasi-newton algorithm based on the trust radius procedure. In order to simulate quasi-2D systems, a vacuum of at least 18 \AA is used to avoid interactions between periodic images in our slab geometry. We choose a 5×5 supercell for graphene, a 2×3 supercell of 1 T' MoTe₂, and we end up with 86 atoms in the hexagonal heterostructure unit cell. Structural relaxations are performed until all components of all forces were reduced below $10^{-3} [R_p/a_0]$, where a_0 is the Bohr radius.

Data availability

The data that support the findings of this study are available from the corresponding authors on reasonable request.

Received: 23 November 2020; Accepted: 6 April 2021;
Published online: 08 June 2021

References

- Soumyanarayanan, A., Reyren, N., Fert, A. & Panagopoulos, C. Emergent phenomena induced by spin-orbit coupling at surfaces and interfaces. *Nature* **539**, 509–517 (2016).
- Manipatruni, S. et al. Scalable energy-efficient magnetoelectric spin-orbit logic. *Nature* **565**, 35–42 (2019).
- Garello, K. et al. SOT-MRAM 300MM integration for low power and ultrafast embedded memories. In *2018 IEEE Symposium on VLSI Circuits* 81–82 (IEEE, 2018). <https://doi.org/10.1109/VLSIC.2018.8502269>
- Manchon, A., Koo, H. C., Nitta, J., Frollov, S. M. & Duine, R. A. New perspectives for Rashba spin-orbit coupling. *Nat. Mater.* **14**, 871–882 (2015).
- Sinova, J., Valenzuela, S. O., Wunderlich, J., Back, C. H. & Jungwirth, T. Spin Hall effects. *Rev. Mod. Phys.* **87**, 1213–1260 (2015).
- Sánchez, J. C. R. et al. Spin-to-charge conversion using Rashba coupling at the interface between non-magnetic materials. *Nat. Commun.* **4**, 2944 (2013).
- Song, Q. et al. Observation of inverse Edelstein effect in Rashba-split 2DEG between SrTiO₃ and LaAlO₃ at room temperature. *Sci. Adv.* **3**, e1602312 (2017).
- Lesne, E. et al. Highly efficient and tunable spin-to-charge conversion through Rashba coupling at oxide interfaces. *Nat. Mater.* **15**, 1261–1266 (2016).
- MacNeill, D. et al. Control of spin-orbit torques through crystal symmetry in WTe₂/ferromagnet bilayers. *Nat. Phys.* **13**, 300–305 (2017).
- Shao, Q. et al. Strong Rashba-Edelstein effect-induced spin-orbit torques in monolayer transition metal dichalcogenide/ferromagnet bilayers. *Nano Lett.* **16**, 7514–7520 (2016).
- Khokhriakov, D., Hoque, A. M., Karpiak, B. & Dash, S. P. Gate-tunable spin-galvanic effect in graphene-topological insulator van der Waals heterostructures at room temperature. *Nat. Commun.* **11**, 3657 (2020).
- Zhao, B., Hoque, A. M., Khokhriakov, D., Karpiak, B. & Dash, S. P. Charge-spin conversion signal in WTe₂ van der Waals hybrid devices with a geometrical design. *Appl. Phys. Lett.* **117**, 242401 (2020).

13. Hoque, A. M., Khokhriakov, D., Karpiak, B. & Dash, S. P. Charge-spin conversion in layered semimetal TaTe₂ and spin injection in van der Waals heterostructures. *Phys. Rev. Res.* **2**, 033204 (2020).
14. Kovács-Krausz, Z. et al. Electrically controlled spin injection from giant Rashba spin-orbit conductor BiTeBr. *Nano Lett.* **20**, 4782–4791 (2020).
15. Zhao, B. et al. Observation of charge to spin conversion in Weyl semimetal WTe₂ at room temperature. *Phys. Rev. Res.* **2**, 013286 (2020).
16. Ghiasi, T. S., Kaverzin, A. A., Blah, P. J. & van Wees, B. J. Charge-to-spin conversion by the Rashba–Edelstein effect in two-dimensional van der Waals heterostructures up to room temperature. *Nano Lett.* **19**, 5959–5966 (2019).
17. Safeer, C. K. et al. Room-temperature spin Hall effect in graphene/MoS₂ van der Waals heterostructures. *Nano Lett.* **19**, 1074–1082 (2019).
18. Dankert, A., Geurs, J., Kamalakar, M. V., Charpentier, S. & Dash, S. P. Room temperature electrical detection of spin polarized currents in topological insulators. *Nano Lett.* **15**, 7976–7981 (2015).
19. Mellnik, A. R. et al. Spin-transfer torque generated by a topological insulator. *Nature* **511**, 449–451 (2014).
20. Johansson, A., Henk, J. & Mertig, I. Edelstein effect in Weyl semimetals. *Phys. Rev. B* **97**, 085417 (2018).
21. Sun, Y., Zhang, Y., Felser, C. & Yan, B. Strong intrinsic spin Hall effect in the TaAs family of Weyl semimetals. *Phys. Rev. Lett.* **117**, 146403 (2016).
22. Das, P. K. et al. Layer-dependent quantum cooperation of electron and hole states in the anomalous semimetal WTe₂. *Nat. Commun.* **7**, 10847 (2016).
23. Weber, A. P. et al. Spin-resolved electronic response to the phase transition in MoTe₂. *Phys. Rev. Lett.* **121**, 156401 (2018).
24. Shi, S. et al. All-electric magnetization switching and Dzyaloshinskii–Moriya interaction in WTe₂/ferromagnet heterostructures. *Nat. Nanotechnol.* **14**, 945–949 (2019).
25. Stiehl, G. M. et al. Layer-dependent spin-orbit torques generated by the centrosymmetric transition metal dichalcogenide β-MoTe₂. *Phys. Rev. B* **100**, 184402 (2019).
26. Zhao, B. et al. Unconventional charge–spin conversion in Weyl-semimetal WTe₂. *Adv. Mater.* <https://doi.org/10.1002/adma.202000818>
27. Safeer, C. K. et al. Large multidirectional spin-to-charge conversion in low-symmetry semimetal MoTe₂ at room temperature. *Nano Lett.* **19**, 8758–8766 (2019).
28. Vila, M. et al. Charge-to-spin interconversion in low-symmetry topological materials. (2020). Preprint at <https://doi.org/10.21203/rs.3.rs-124172/v1> (2020)
29. Khokhriakov, D. et al. Tailoring emergent spin phenomena in Dirac material heterostructures. *Sci. Adv.* **4**, eaat9349 (2018).
30. Cummings, A. W., Garcia, J. H., Fabian, J. & Roche, S. Giant spin lifetime anisotropy in graphene induced by proximity effects. *Phys. Rev. Lett.* **119**, 206601 (2017).
31. Zhang, J., Triola, C. & Rossi, E. Proximity effect in graphene–topological-insulator heterostructures. *Phys. Rev. Lett.* **112**, 096802 (2014).
32. Song, K. et al. Spin proximity effects in graphene/topological insulator heterostructures. *Nano Lett.* **18**, 2033–2039 (2018).
33. Offidani, M., Milletari, M., Raimondi, R. & Ferreira, A. Optimal charge-to-spin conversion in graphene on transition-metal dichalcogenides. *Phys. Rev. Lett.* **119**, 196801 (2017).
34. Li, L. et al. Gate-tunable reversible Rashba–Edelstein effect in a few-layer graphene/2H-TaS₂ heterostructure at room temperature. *ACS Nano* **14**, 5251–5259 (2020).
35. Benítez, L. A. et al. Tunable room-temperature spin galvanic and spin Hall effects in van der Waals heterostructures. *Nat. Mater.* **19**, 170–175 (2020).
36. Jiang, J. et al. Signature of type-II Weyl semimetal phase in MoTe₂. *Nat. Commun.* **8**, 13973 (2017).
37. Deng, K. et al. Experimental observation of topological Fermi arcs in type-II Weyl semimetal MoTe₂. *Nat. Phys.* **12**, 1105–1110 (2016).
38. Grzeszczyk, M. et al. Raman scattering of few-layers MoTe₂. *2D Mater.* **3**, 025010 (2016).
39. Gmitra, M. & Fabian, J. Graphene on transition-metal dichalcogenides: a platform for proximity spin-orbit physics and optospintronics. *Phys. Rev. B* **92**, 155403 (2015).
40. Wang, Z. et al. Origin and magnitude of ‘Designer’ spin-orbit interaction in graphene on semiconducting transition metal dichalcogenides. *Phys. Rev. X* **6**, 041020 (2016).
41. Khokhriakov, D., Karpiak, B., Hoque, A. M. & Dash, S. P. Two-dimensional spintronic circuit architectures on large scale graphene. *Carbon N. Y.* **161**, 892–899 (2019).
42. Khokhriakov, D. et al. Robust spin interconnect with isotropic spin dynamics in chemical vapor deposited graphene layers and boundaries. *ACS Nano* (2020). <https://doi.org/10.1021/acsnano.0c07163>
43. Kimura, T., Otani, Y., Sato, T., Takahashi, S. & Maekawa, S. Room-temperature reversible spin Hall effect. *Phys. Rev. Lett.* **98**, 156601 (2007).
44. Hasan, M. Z. & Kane, C. L. Colloquium: topological insulators. *Rev. Mod. Phys.* **82**, 3045–3067 (2010).
45. Giannozzi, P. et al. Quantum ESPRESSO: a modular and open-source software project for quantum simulations of materials. *J. Phys. Condens. Matter* **21**, 395502 (2009).
46. Hohenberg, P. & Kohn, W. Inhomogeneous electron gas. *Phys. Rev.* **136**, B864–B871 (1964).
47. Milletari, M., Offidani, M., Ferreira, A. & Raimondi, R. Covariant conservation laws and the spin Hall effect in Dirac-Rashba systems. *Phys. Rev. Lett.* **119**, 246801 (2017).
48. Karpiak, B. et al. 1D ferromagnetic edge contacts to 2D graphene/h-BN heterostructures. *2D Mater.* **5**, 014001 (2017).
49. Karpiak, B. et al. Magnetic proximity in a van der Waals heterostructure of magnetic insulator and graphene. *2D Mater.* **7**, 015026 (2020).
50. Kresse, G. & Joubert, D. From ultrasoft pseudopotentials to the projector augmented-wave method. *Phys. Rev. B* **59**, 1758–1775 (1999).
51. Perdew, J. P., Burke, K. & Ernzerhof, M. Generalized gradient approximation made simple. *Phys. Rev. Lett.* **77**, 3865–3868 (1996).
52. Barone, V. et al. Role and effective treatment of dispersive forces in materials: polyethylene and graphite crystals as test cases. *J. Comput. Chem.* **30**, 934–939 (2009).
53. Grimme, S. Semiempirical GGA-type density functional constructed with a long-range dispersion correction. *J. Comput. Chem.* **27**, 1787–1799 (2006).

Acknowledgements

The authors acknowledge financial support from the European Union Graphene Flagship (Core 2 No. 785219 and Core 3 No. 881603), EU FlagEra project (from Swedish Research Council VR No. 2015-06813), Swedish Research Council VR project grants (No. 2016-03658), 2D Tech VINNOVA center, Graphene center, and the EI Nano and AoA Materials program at Chalmers University of Technology. KZ and JF also acknowledge support by the Deutsche Forschungsgemeinschaft (DFG, German Research Foundation) SFB 1277 (Project-ID 314695032). We acknowledge the staff at Quantum Device Physics and Nanofabrication laboratory in our department at the Chalmers University of Technology.

Author contributions

S.P.D. and A.M.H. conceived the idea and designed the experiments. A.M.H. fabricated and measured the devices. D.K., B.K., B.Z. and S.P.D. contributed to some device fabrication and measurements. A.M.H. and S.P.D. analyzed the experimental data and wrote the manuscript. DFT calculations were carried out by K.Z. and J.F. All authors participated in the discussions and manuscript preparation. S.P.D. supervised the research and managed the research project.

Funding

Open access funding provided by Chalmers University of Technology.

Competing interests

The authors declare no competing interests.

Additional information

Supplementary information The online version contains supplementary material available at <https://doi.org/10.1038/s42005-021-00611-6>.

Correspondence and requests for materials should be addressed to S.P.D.

Reprints and permission information is available at <http://www.nature.com/reprints>

Publisher's note Springer Nature remains neutral with regard to jurisdictional claims in published maps and institutional affiliations.



Open Access This article is licensed under a Creative Commons Attribution 4.0 International License, which permits use, sharing, adaptation, distribution and reproduction in any medium or format, as long as you give appropriate credit to the original author(s) and the source, provide a link to the Creative Commons license, and indicate if changes were made. The images or other third party material in this article are included in the article's Creative Commons license, unless indicated otherwise in a credit line to the material. If material is not included in the article's Creative Commons license and your intended use is not permitted by statutory regulation or exceeds the permitted use, you will need to obtain permission directly from the copyright holder. To view a copy of this license, visit <http://creativecommons.org/licenses/by/4.0/>.

© The Author(s) 2021